Direct measurement of emittance using the MICE scintillating fibre tracker

V. Blackmore, K. Long

The Muon Ionization Cooling Experiment (MICE) collaboration seeks to demonstrate the feasibility of ionization cooling, the technique by which it is proposed to cool the muon beam at a future neutrino factory or muon collider. The muon beam emittance is derived from an ensemble of muons assembled from muons that pass through the experiment. A pure muon beam is selected using a particle identification system that can reject efficiently both pions and electrons. The position and momentum of each muon is measured using a high-precision scintillating-fibre tracker in a 4 T solenoidal magnetic field. This paper reports the techniques used to reconstruct the emittance of the muon beam in the upstream spectrometer and reports the emittance of the muon beam as a function of muon-beam momentum.

1 Introduction

Stored muon beams have been proposed as the source of neutrinos at a neutrino factory [1, 2] and as the means to deliver multi-TeV lepton-antilepton collisions at a muon collider [3, 4]. In such facilities the muon beam is produced from the decay of pions generated by a high-power proton beam striking a target. The tertiary muon beam occupies a large volume in phase space. To optimise the muon yield while maintaining a suitably small aperture in the muon-acceleration system requires that the muon beam be "cooled" (i.e., its phase-space volume reduced) prior to acceleration.

A muon is short-lived, decaying with a lifetime of 2.2 μs in its rest frame. Therefore, beam manipulation at low energy (≤ 1 GeV) must be carried out rapidly. Four cooling techniques are in use at particle accelerators: synchrotron-radiation cooling [5]; laser cooling [6–8]; stochastic cooling [9]; and electron cooling [10]. In each case, the time taken to cool the beam is long compared to the muon lifetime. In contrast, the cooling time associated with ionization cooling, in which the energy of a muon beam is reduced as it passes through a material, the absorber, and is subsequently accelerated, is short enough to allow the muon beam to be cooled efficiently with modest decay losses. Ionization cooling is therefore the technique by which it is proposed to reduce the muon-beam phase space in the neutrino factory and muon collider [11–13]. This technique has never been demonstrated experimentally and such a demonstration is essential for the development of future high-brightness muon accelerators.

The international Muon Ionization Cooling Experiment (MICE) has been designed [] to perform a full demonstration of transverse ionization cooling. The particle density in the ionization-cooling channels conceived for the neutrino factory or muon collider [] is low enough for collective effects such as space charge to be neglected. This allows the MICE experiment to record muon trajectories one particle at a time. An ensemble of muon trajectories is assembled offline so that beam properties, such as emittance, can be calculated from the ensemble. The MICE collaboration has constructed two solenoidal spectrometers, one placed upstream, the other downstream, of the cooling cell. This paper describes the techniques used to reconstruct emittance in the spectrometers and presents a measurement of emittance of a variety of beams in the upstream spectrometer.

2 Calculation of emittance

A beam travelling through a portion of an accelerator may be described in terms of an ensemble of particles. Consider a beam that propagates in the positive z direction of a right-handed Cartesian coordinate system, (x, y, z). The position of the i^{th} particle in the ensemble, $\mathbf{r}_i = (x_i, y_i, z_i)$, and its momentum, $\mathbf{p}_i = (p_{xi}, p_{yi}, p_{zi})$, then define the coordinates of the particle in the six dimensions of phase space. The emittance of the ensemble is the RMS spread of the phase-space coordinates of the particles about their barycentre in phase space. The normalised transverse emittance, ϵ_N, of the ensemble is given by:

$$\varepsilon_N = \frac{1}{m_\mu} \sqrt[4]{\det \mathcal{C}} \; ; \tag{1}$$

where m_μ is the rest mass of the muon, $\mathcal{C}$ is the four-dimensional covariance matrix defined by:

$$\mathcal{C} = \begin{pmatrix} \sigma_{xx} & \sigma_{xy} & \sigma_{xp_x} & \sigma_{xp_y} \\ \sigma_{xy} & \sigma_{yy} & \sigma_{yp_x} & \sigma_{yp_y} \\ \sigma_{xp_x} & \sigma_{yp_x} & \sigma_{p_xp_x} & \sigma_{p_xp_y} \\ \sigma_{xp_y} & \sigma_{yp_y} & \sigma_{p_xp_y} & \sigma_{p_yp_y} \end{pmatrix} \; ; \tag{2}$$

and:

$$\sigma_{\alpha\beta} = \frac{\left(\Sigma_i^N \alpha_i \beta_i\right) - \left(\Sigma_i^N \alpha_i\right)\left(\Sigma_i^N \beta_i\right)}{N} \; . \tag{3}$$

The MICE experiment is operated such that muons pass through the experiment one at a time. The phase-space coordinates of each muon is reconstructed and an ensemble of muons that is representative of the muon beam is assembled. The normalised transverse emittance of the ensemble is then calculated by evaluating the sums necessary to construct the covariance matrix $\mathcal{C}$ and the normalised transverse emittance is calculated using equation 1.

3 The Muon Ionization Cooling Experiment

The muons for MICE come from the decay of pions produced at an internal target dipping directly into the circulating proton beam in the ISIS synchrotron at the Rutherford Appleton Laboratory (RAL) [14, 15]. The burst of particles resulting from one target dip is referred to as a "spill". A beam line of 9 quadrupoles, 2 dipoles and a superconducting "decay solenoid" collects and transports the momentum-selected beam into the experiment [16]. The small fraction of pions that remain in the beam may be rejected during analysis using the time-of-flight hodoscopes and Cherenkov counters that are installed in the beam line upstream of the experiment [17]. A diffuser is installed at the upstream end of the experiment to vary the initial emittance of the beam.

A schematic diagram of the experiment is shown in figure 1. It contains an absorber/focus-coil (AFC) module sandwiched between two spectrometer-solenoid modules. The focus-coil (FC) module has two separate windings that can be operated either with the same or in opposed polarity. A lithium-hydride (LiH) or liquid-hydrogen (LH_2) absorber can be placed at the centre of the FC module.

The emittance is measured upstream and downstream of the cooling cell using scintillating-fibre tracking detectors [21] immersed in the uniform magnetic field provided by three superconducting coils (E1, C, E2). The trackers are used to reconstruct the trajectories of individual muons at the entrance and exit of the cooling cell. The reconstructed tracks are combined with information from instrumentation upstream and downstream of the spectrometer modules to measure the muon-beam emittance at the upstream and downstream tracker reference planes. The instrumentation upstream and downstream of the spectrometer modules serves to select

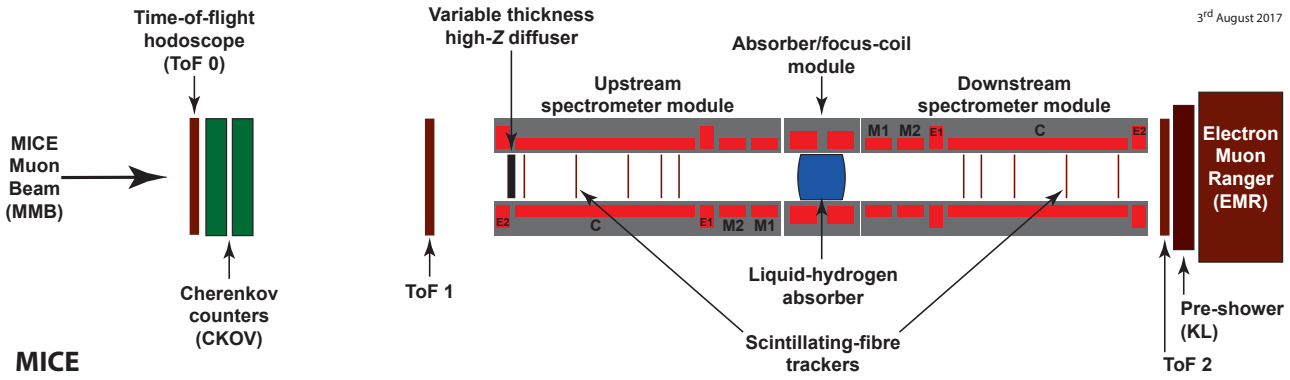

Figure 1: Schematic diagram of the configuration of the experiment. The red rectangles represent the solenoids. The individual coils in the spectrometer solenoids are labelled E1, C, E2, M1 and M2. The various detectors (time-of-flight hodoscopes [18, 19], Cerenkov counters [20], scintillating-fibre trackers [21], KLOE Light (KL) calorimeter [16, 22], electron muon ranger [23]) used to characterise the beam are also represented.

a pure sample of muons. Time-of-flight hodoscopes are used to determine the time at which the muon crosses the RF cavities. The spectrometer-solenoid magnets also contain two superconducting "matching" coils (M1, M2) that are used to match the optics between the uniform field region and the neighbouring FC.

4 MICE Muon Beam

The MICE Muon Beam, shown schematically in figure 2, is capable of delivering beams with normalised transverse emittance in the range $3 \leq \epsilon_N \leq 10\pi$ mm $\cdot$ rad and mean momentum in the range $140 \leq p_\mu \leq 240$ MeV/c with a root-mean-squared (RMS) momentum spread of $\sim$20 MeV/c [16]. A pneumatically operated "diffuser", consisting of tungsten and brass irises of various thicknesses, is placed at the entrance to the upstream spectrometer solenoid to generate the required range of emittance.

Pions produced by the momentary insertion of a titanium target [14, 15] into the 800 MeV ISIS proton beam are captured using a quadrupole triplet (Q1–3) and transported to a first dipole magnet (D1), which selects particles of a desired momentum bite into the 5 T decay solenoid (DS). Muons produced in pion decay in the DS are momentum-selected using a second dipole magnet (D2) and focused onto the diffuser by a quadrupole channel (Q4–6 and Q7–9). In positive-beam running, a borated polyethylene absorber of variable thickness is inserted into the beam just downstream of the DS in order to suppress the high rate of protons that are produced at the target [24].

The composition and momentum spectra of the beams delivered to MICE are determined by the interplay between the two bending magnets D1 and D2. In "$\pi \to \mu$" or "muon" mode, D2 is set to half the momentum of D1, selecting backward-going muons in the pion rest frame and producing an almost pure muon beam. The nominal values of the beam momenta, p_μ, are those evaluated at the centre of the central LiH absorber, taking into account the energy lost by the particles along the muon beam in the TOF and Cherenkov detectors, the proton absorber (for positive polarity beams), the diffuser and the air along the particle trajectories. For example, a momentum at D2, $p_{D2} = 238$ MeV/c, implies a momentum value $p_\mu = 200$ MeV/c at the centre of the central absorber.

Data were taken in October 2015 in muon mode at a nominal momentum of 200 MeV/c. To characterise the properties of the beam accepted by the upstream solenoid, all diffuser irises were withdrawn from the beam. The upstream spectrometer solenoid (SSU) energised such that a uniform field of 4 T was produced in the

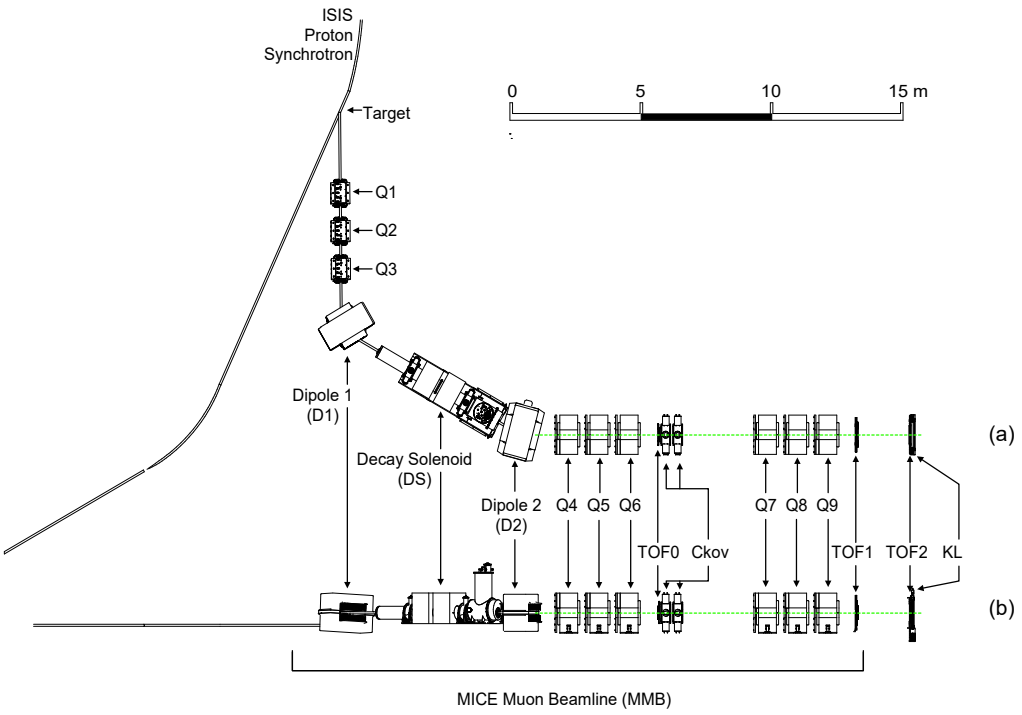

Figure 2: (a) Top view of the MICE Muon Beam and its instrumentation for the pion contamination measurement. (b) Side view of the MICE Muon Beam.

tracking region, all other coils were unpowered.

5 Simulation

Monte Carlo simulations were used to determine the accuracy of the kinematic reconstruction, to evaluate the efficiency for of the response of the scintillating-fibre tracker and to study systematic uncertainties. A sufficient number of events was generated to ensure that statistical uncertainties from the simulations were negligible in comparison to those of the data.

The beam impinging on TOF0 was simulated using G4beamline []. Particles produced by protons striking the target were tracked through the MICE Muon Beam taking into account all material in and surrounding the beam line and using realistic models of the field and apertures of the various magnets. The G4beamline-simulation was tuned to reproduce adequately the observed particle distributions at TOF0.

The MICE User Analysis Software (MAUS) [] package was used to simulate the passage of particles through the MICE magnetic lattice and the response of the instrumentation. In addition to simulation, MAUS also provides a framework for data analysis. MAUS is used for offline analysis and to provide fast real-time detector reconstruction and data visualisation during MICE running. MAUS uses GEANT4 [25, 26] for beam propagation and the simulation of detector response. The events generated were subjected to the same trigger requirements as the data and processed by the same reconstruction programs. ROOT [27] is used for data visualisation and for data storage.

6 Beam selection

The experiment is read out at the end of each spill. This makes it necessary to buffer digital information related to the passage of the particles through the experiment in the front-end electronics (for a description of the MICE trigger and data-acquisition system see []). For the data presented here, the digitisation of the analogue signals received from the detectors was triggered by a coincidence of signals in the two PMTs serving a single scintillator slab in TOF1. Any slab in TOF1 could generate a trigger.

The following cuts were used to select muons passing through the upstream tracker:

- *One reconstructed space-point in TOF0 and TOF1*: Each TOF hodoscope is composed of two perpendicular planes of scintillator slabs arranged to measure the x and y coordinates. A space-point is formed from the intersection of hits in the x and y projections. Figure 3 shows hit multiplicity in TOF1 plotted against the hit multiplicity in TOF0. The sample is dominated by events with one space-point in both TOF0 and TOF1. This cut removes events in which two particles enter the experiment within the trigger window;
- *Time of flight between TOF0 and TOF1, t_{01}, in the range $27 < t_{01} < 33\,ns$*: Figure 3 shows the time of flight distribution for muons passing all cuts other than the time-of-flight cut. The cut on t_{01} removes positrons and a small number of pions that contribute to the sample at large t_{01};
- *A single track reconstructed in the upstream tracker with a track-fit χ^2 satisfying $\frac{\chi^2}{N_{\rm DOF}} < 4$: $N_{\rm DOF}$* is the number of degrees of freedom. The distribution of $\frac{\chi^2}{N_{\rm DOF}}$ is shown in figure 3. This cut removes events with poorly reconstructed tracks. In rare cases, more than one particle may pass through the same pixel in TOF0 and TOF1 during the trigger window. This cut removes such events;
- *Track contained within the fiducial volume of the tracker*: The active area of each tracker station extends to a radius of 150 mm. The radius of the track at each tracker station, $R_{\rm stn}$, is required to satisfy $R_{\rm stn} < 150$ mm. To ensure the track does not leave and then re-enter the fiducial volume, the track radius is evaluated at 50 mm intervals between the stations. If the track radius exceeds 150 mm at any of these positions, the event is rejected; and
- *Track radius at the diffuser, $R_{\rm diff} < 80\,mm$*: Muons that pass through the material of the absorber, which includes the retracted irises, lose a substantial amount of energy. Such muons may re-enter the tracking volume and be reconstructed but have properties that are no longer characteristic of the incident muon beam. The inner radius of the diffuser mechanism (100 mm) defines the transverse acceptance of the beam injected into the experiment. Back-extrapolation of tracks to the exit of the diffuser yields a measurement of $R_{\rm diff}$ with a resolution of $\sigma_{R_{\rm diff}} = 1.8$ mm. Figure 3 shows the distribution of $R_{\rm diff}$. The cut on $R_{\rm diff}$ accepts particles that passed within $3\sigma_{R_{\rm diff}}$ of the inner radius of the diffuser.

A total of 20 962 events pass the cuts listed above (Table 1). Data distributions are compared to the distributions obtained using the MAUS simulation in figure 3. The distribution of the time of flight between TOF0 and TOF1 is peaked towards slightly longer times in the simulation than in the data. This is related to the imperfect simulation of the distribution of longitudinal momentum of particles in the beam (see below). The distribution of $\frac{\chi^2}{N_{\rm DOF}}$ is broader and peaked at slightly larger values in the data than in the simulation. Despite this minor disagreements, the agreement between the simulation and data is sufficiently good to give confidence that a clean sample of muons is selected.

Figure 4 shows t_{01} plotted as a function of $p_{\rm tk}$, the momentum reconstructed in SSU. The same distribution obtained from the simulation is also shown. The bulk of the data is consistent with the muon hypothesis. Events lying above the upper solid black lines in figure 4 are ascribed to the passage of pions and are removed from the analysis. The population of events lying below the lower solid-black line arise from muons that are poorly reconstructed or have passed through inactive material upstream of the tracker and have lost momentum. These muons are also removed from the analysis. ?? events are removed by this requirement, leaving a total of ?? ???

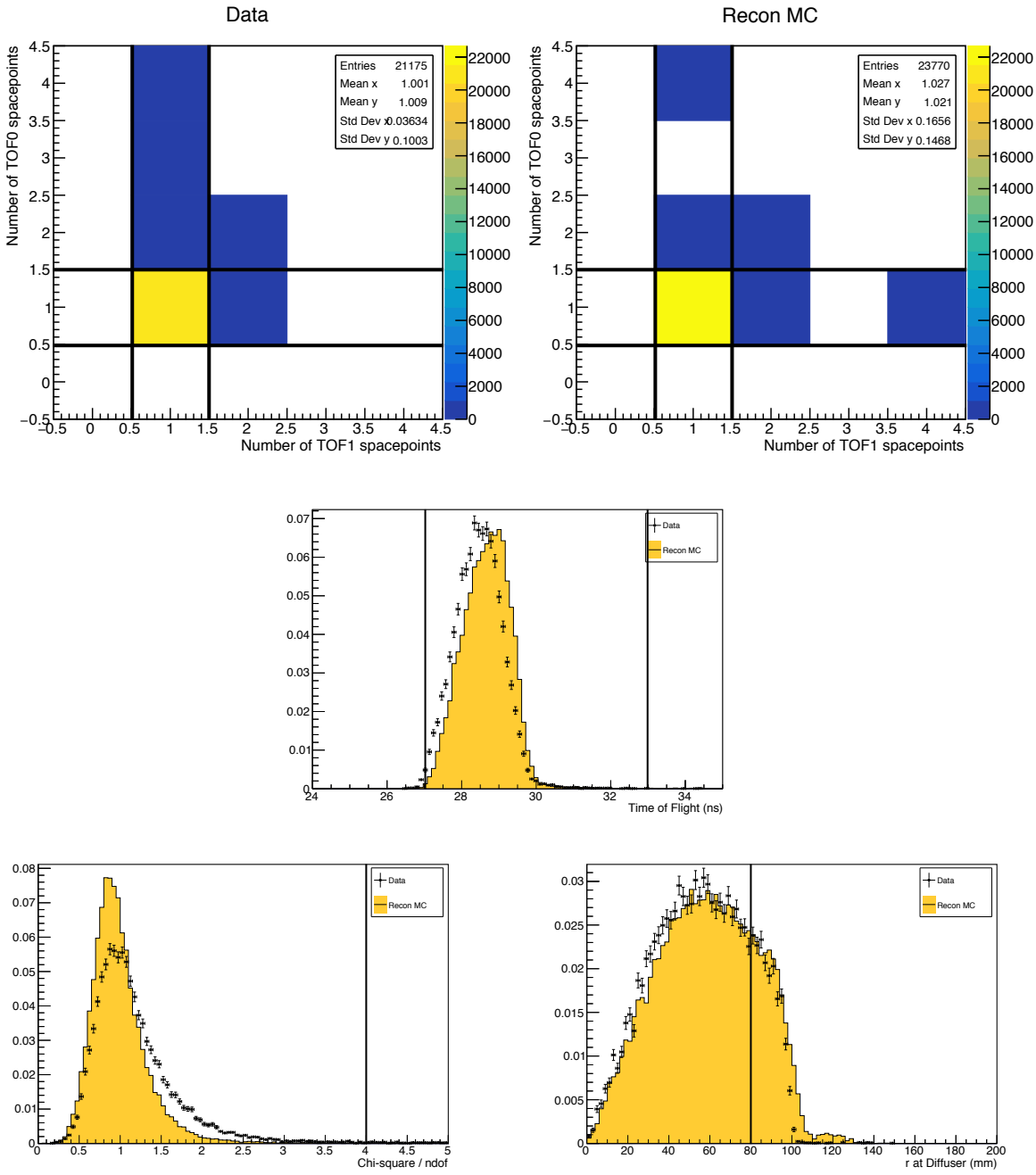

Figure 3: Distribution of the quantities used to select the sample used to reconstruct the emittance of the beam. Top left: the number of space-points in TOF1 plotted against the number of space-points in TOF0; Top right: distribution of t_{01}; Bottom left: distribution of $\frac{\chi^2}{N_{\mathrm{DOF}}}$; and Bottom right: distribution of R_{diff}. In each case the data is shown as the solid circles or, in the case of the space-point distributions in TOF1 and TOF0, the black squares and the distribution obtained with the MAUS simulation is shown as the solid yellow histogram. The solid black lines indicate the position of the cuts made on the various quantities. Events enter the plots if all cuts other than the cut under examination are passed.

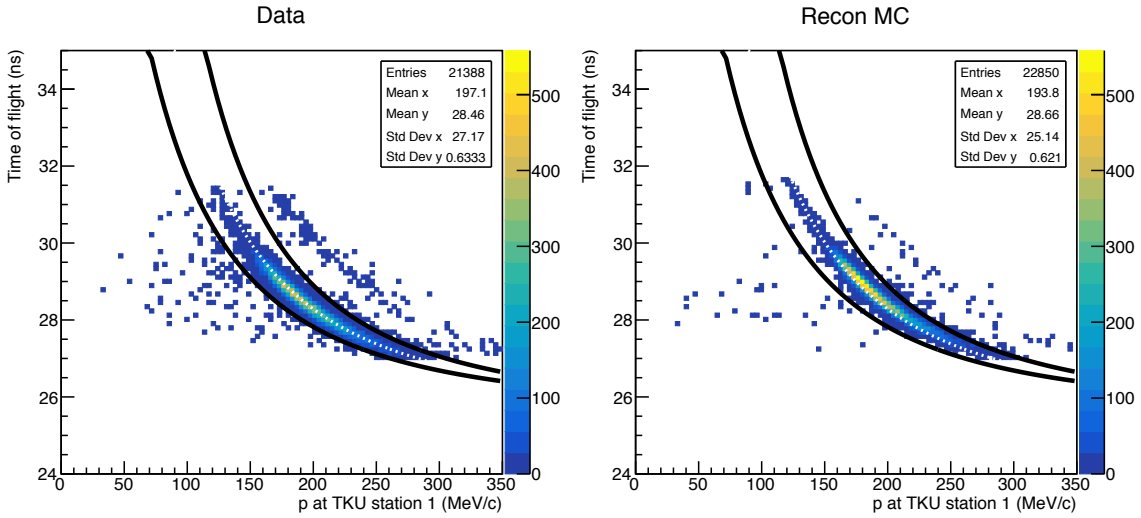

Figure 4: Time of flight between TOF0 and TOF1 (t_{01}) plotted as a function of the muon momentum, p_{tk}, measured in the upstream tracker. The (white) dotted line is the trajectory of a muon that loses the mean momentum (20 MeV/c) between TOF1 and the tracker. (Left) Data, (Right) Reconstructed Monte Carlo.

Table 1: The number of particles that pass each selection criteria. A total of 20 962 particles pass all of the described cuts.

Cut	No. particles that pass
None	53 452
One space-point in TOF0 and TOF1	37 746
Time of flight in range 27—33 ns	37 213
Single reconstructed track with $\frac{\chi^2}{N_{\mathrm{DOF}}} < 4$	39 942
Track within fiducial volume of tracker	52 011
Tracked radius at diffuser $<$ 80 mm	35 837
All	20 962

events.

7 Results

7.1 Phase-space projections

The distributions in $x, y, p_x, p_y, p_z, p_\perp^2, p_\perp$ (where $p_\perp^2 = p_x^2 + p_y^2$) and $p = \sqrt{p_x^2 + p_y^2 + p_z^2}$ are shown in figure 5. The distributions are plotted at the reference surface of the upstream tracker; the most downstream surface of the scintillating-fibre plane closest to the absorber/focus-coil module. The longitudinal momentum of the muons that make up the beam lie within the range $140 \lesssim p_z \lesssim 260$ MeV/c. The results of the MAUS simulation, which are also shown in figure 5, give a good description of the data. In the case of the longitudinal component of momentum, p_z, the data is peaked to slightly larger values than the simulation. The difference is small and is reflected in the distribution of the total momentum, p. The distributions of the components of the transverse phase space (x, y, p_x, p_y) are well described by the simulation.

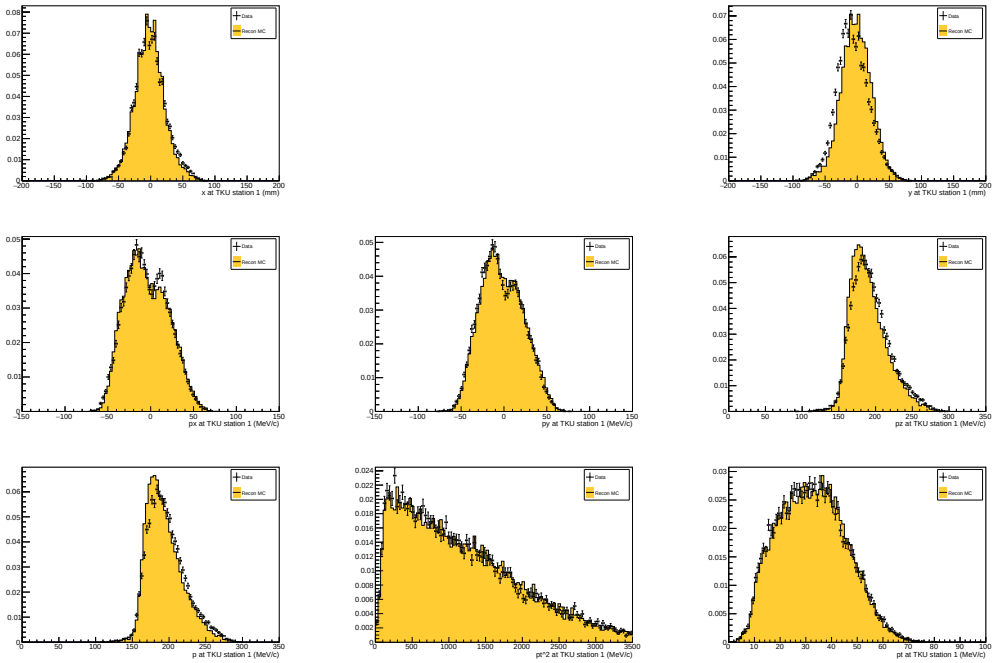

Figure 5: Position and momentum distributions of muons reconstructed at the reference surface of the upstream tracker. The top left and top right panels show the distributions of x and y respectively. The distributions of components of the muon momentum are shown in the middle row; p_x in the left-middle panel, p_y in the centre middle panel and p_z in the right-middle panel. The distribution of the total momentum, p, is shown in the bottom-left panel. The distributions of the transverse momentum squared, $p_\perp^2 = p_x^2 + p_y^2$, and $p_\perp$ are shown in the bottom-middle and bottom-right panels respectively. The data is shown as the solid circles while the results of the MAUS simulation are shown as the yellow histogram.

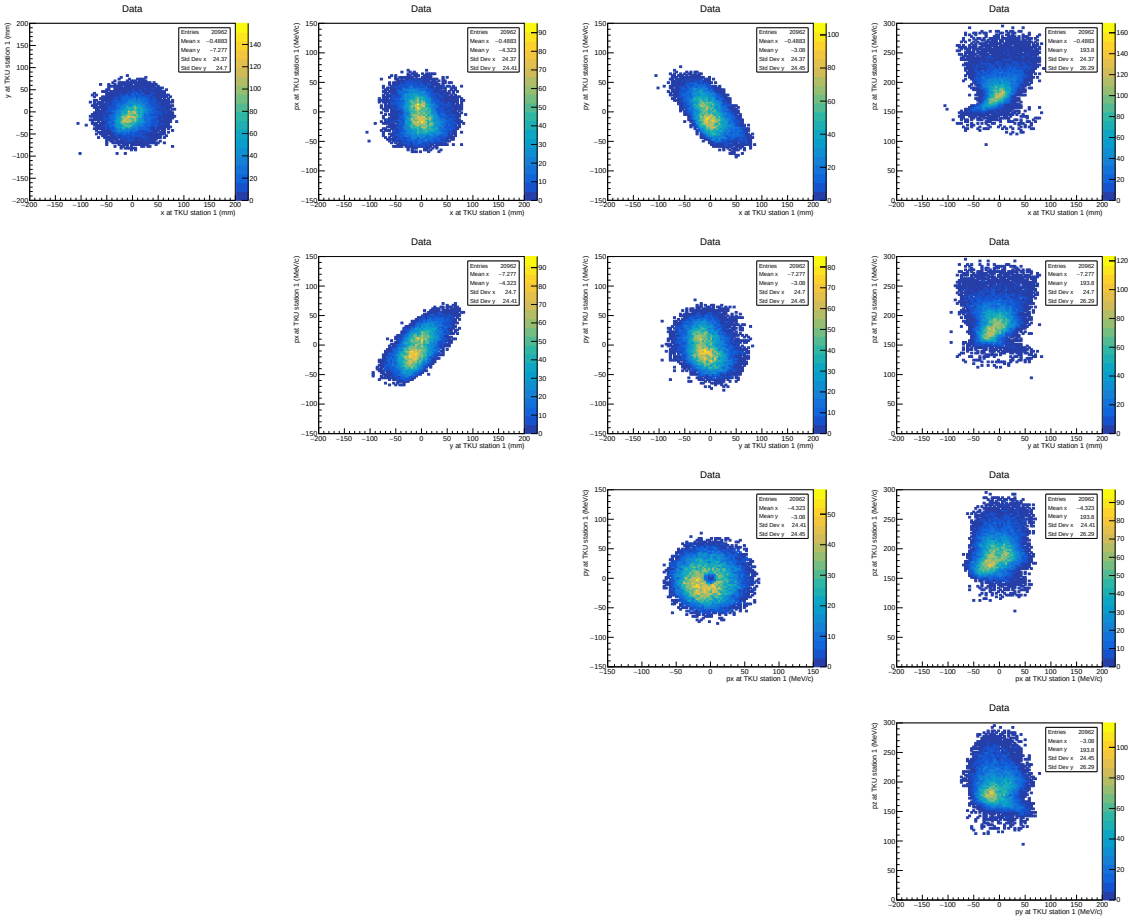

Figure 6: Phase space occupied by muons transported through the MMB to the reference plane of the upstream Tracker.

The phase space occupied by the beam selected by the procedure described in section 6 is shown in figure 6. The distributions are plotted at the reference surface of the upstream tracker. The beam is well centred in the (x, y) plane. Correlations are apparent that couple the position and momentum components in the transverse plane. The transverse position and momentum coordinates are also seen to be correlated with longitudinal momentum. The dispersion in the beam is discussed further in section 7.2.

7.2 Dispersion and binning in longitudinal momentum

Momentum selection at D2 introduces a correlation between position and momentum. Figure 8 shows the mean x, y of the muon beam as a function of p_z in 10 MeV/c p_z bins. The mean horizontal position systematically shifts to positive x as the momentum of the sample increases. The variation seen in the mean vertical position is due to the helical trajectory particles take coupled with the offset horizontal position of the particles when entering the solenoid field. The mean radial position r ($r = \sqrt{x^2 + y^2}$) is also shown as a function of p_z. The mean r increases as p_z increases reflecting the increase in the mean x with p_z. The mean $p_\perp$ is plotted as a function of p_z in figure 8. For p_z greater than $\approx$ 170 MeV, the mean $p_\perp$ rises with increasing p_z. For $p_z \lesssim 170$ MeV/c, the mean $p_\perp$ rises rapidly as p_z falls. The dependence of the mean $p_\perp$ on p_z for $p_z <$ 170 MeV/c is related to the negative correlation between p_y and p_z for values of p_z below 170 MeV/c, see figure 6.

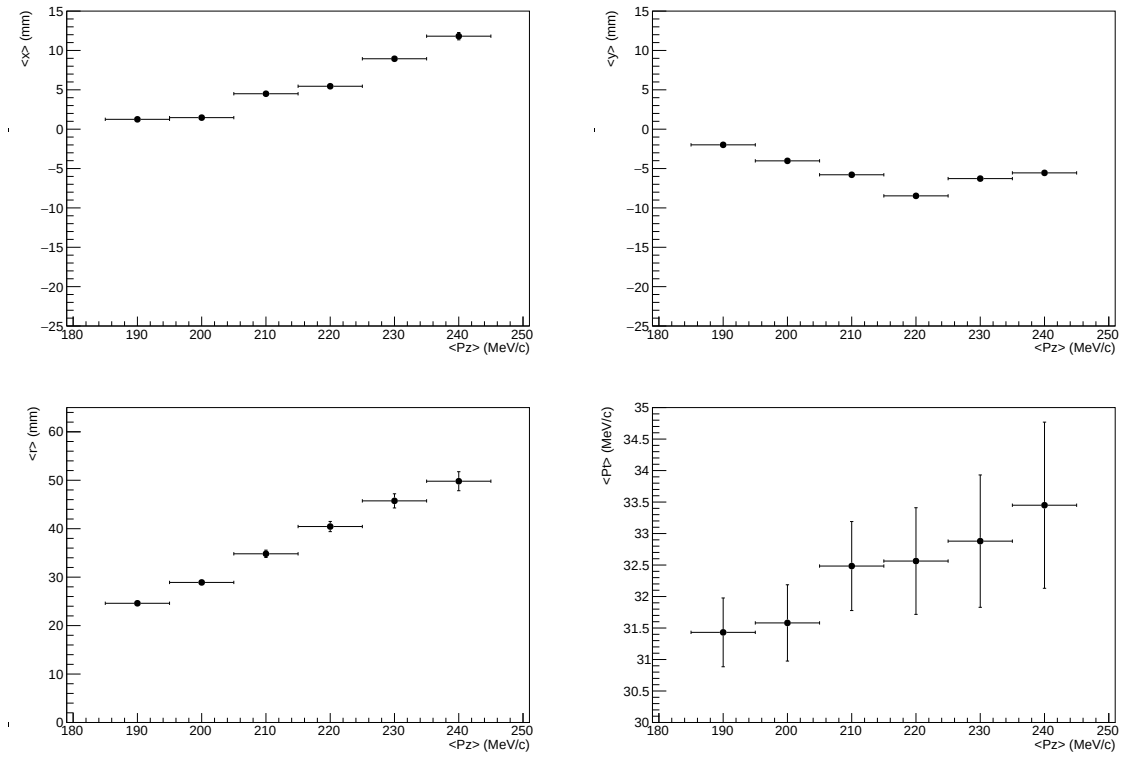

Figure 7: Variation in mean particle parameters as a function of p_z. Top left: x, top right: y, bottom left: mean track radius, r, bottom right: mean $p_\perp$.

The kinematic region over which the emittance has been determined is $175 \leq p_z \leq 245\,\text{MeV/c}$ since the dependence of the mean $p_\perp$ on p_z changes qualitatively for $p_z \lesssim 170\,\text{MeV/c}$ and the beam contains relatively few events with $p_z \gtrsim 250\,\text{MeV/c}$. The size of the bins of p_z used to report the reconstructed emittance were chosen commensurate with the resolution. The p_z resolution is plotted as a function of p_z in figure **??**. The resolution is $\sim 4\,\text{MeV/c}$ and is approximately independent of p_z. A bin width of 10 MeV/c was therefore chosen. The number of events per bin is shown in figure **??**. The number of events per bin varies from $\sim???$ for $p_z \sim???\,\text{MeV/c}$ to $\sim???$ for $p_z \sim???$. The efficiency (defined as the number of events generated and reconstructed in a bin after all selection cuts divided by the number of events that were generated in that bin) is also shown in figure **??**. The efficiency is always greater than ??%. The purity (defined as the number of events reconstructed and generated in a bin after all selection cuts divided by the total number of events reconstructed in that bin), also shown in figure **??**, is always greater than ??%.

Two more paras for this section:

- Comment on why no correction to the measured emittance is necessary! Chris H is preparing a plot of resolution in p_x and p_y as a function of p_z. I'm hoping that this is sufficient documentation to say we can ignore for now; and
- Comment on how statistical uncertainties are calculated. I assume you're just doing Poisson errors based on the population in the bin. But, we should write that down.

7.3 Systematic uncertainties

Systematic uncertainties related to the beam selection were estimated by varying the cut values by an amount corresponding to the RMS resolution of the quantity in question. Systematic uncertainties related to possible biases in calibration constants were evaluated by varying the calibration constant in line with its resolution. Systematic uncertainties related to the reconstruction algorithms were evaluated using the MAUS simulation. The positive and negative deviations from the nominal emittance were added in quadrature separately to obtain the total positive and negative systematic uncertainly. Sources of uncorrelated and correlated uncertainties are discussed in detail below.

7.3.1 Uncorrelated systematic uncertainties

List!

7.3.2 Correlated systematic uncertainties

List!

7.4 Emittance

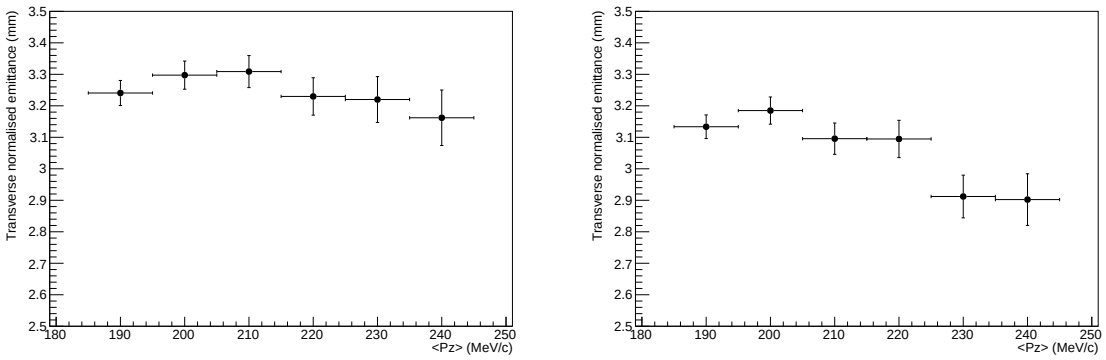

Figure 8: Variation in normalised transverse emittance as a function of p_z. Error bars are statistical. Left: Reconstructed data, Right: Reconstructed Monte Carlo.

References

[1] S. Geer, "Neutrino beams from muon storage rings: Characteristics and physics potential," *Phys. Rev.* **D57** (1998) 6989–6997, arXiv:hep-ph/9712290.

[2] M. Apollonio *et al.*, "Oscillation physics with a neutrino factory," hep-ph/0210192.

[3] D. V. Neuffer and R. B. Palmer, "A High-Energy High-Luminosity $\mu^+ - \mu^-$ Collider," *Conf. Proc.* **C940627** (1995) 52–54.

[4] R. B. Palmer, "Muon Colliders," *Rev. Accel. Sci. Tech.* **7** (2014) 137–159.

[5] S. Y. Lee, *Accelerator Physics (Third Edition)*. World Scientific Publishing Co, 2012.

[6] S. Schröder, R. Klein, N. Boos, M. Gerhard, R. Grieser, G. Huber, A. Karafillidis, M. Krieg, N. Schmidt, T. Kühl, R. Neumann, V. Balykin, M. Grieser, D. Habs, E. Jaeschke, D. Krämer, M. Kristensen, M. Music, W. Petrich, D. Schwalm, P. Sigray, M. Steck, B. Wanner, and A. Wolf, "First laser cooling of relativistic ions in a storage ring," *Phys. Rev. Lett.* **64** (Jun, 1990) 2901–2904. http://link.aps.org/doi/10.1103/PhysRevLett.64.2901.

[7] J. S. Hangst, M. Kristensen, J. S. Nielsen, O. Poulsen, J. P. Schiffer, and P. Shi, "Laser cooling of a stored ion beam to 1 mk," *Phys. Rev. Lett.* **67** (Sep, 1991) 1238–1241. http://link.aps.org/doi/10.1103/PhysRevLett.67.1238.

[8] P. J. Channell, "Laser cooling of heavy ion beams," *Journal of Applied Physics* **52** no. 6, (1981) 3791–3793, http://dx.doi.org/10.1063/1.329218. http://dx.doi.org/10.1063/1.329218.

[9] J. Marriner, "Stochastic cooling overview," *Nucl. Instrum. Meth.* **A532** (2004) 11–18, arXiv:physics/0308044 [physics].

[10] V. V. Parkhomchuk and A. N. Skrinsky, "Electron cooling: 35 years of development," *Physics-Uspekhi* **43** no. 5, (2000) 433–452. http://stacks.iop.org/1063-7869/43/i=5/a=R01.

[11] A. N. Skrinsky and V. V. Parkhomchuk, "Cooling Methods for Beams of Charged Particles. (In Russian)," *Sov. J. Part. Nucl.* **12** (1981) 223–247. [Fiz. Elem. Chast. Atom. Yadra12,557(1981)].

[12] D. Neuffer, "Principles and Applications of Muon Cooling," *Conf.Proc.* **C830811** (1983) 481.

[13] D. Neuffer, "Principles and Applications of Muon Cooling," *Part. Accel.* **14** (1983) 75–90.

[14] C. N. Booth *et al.*, "The design, construction and performance of the MICE target," *JINST* **8** (2013) P03006, arXiv:1211.6343 [physics.ins-det].

[15] C. N. Booth *et al.*, "The design and performance of an improved target for MICE," *JINST* **11** no. 05, (2016) P05006, arXiv:1603.07143 [physics.ins-det].

[16] **MICE collaboration** Collaboration, M. Bogomilov *et al.*, "The MICE Muon Beam on ISIS and the beam-line instrumentation of the Muon Ionization Cooling Experiment," *JINST* **7** (2012) P05009, arXiv:1203.4089 [physics.acc-ph].

[17] **MICE** Collaboration, D. Adams *et al.*, "Characterisation of the muon beams for the Muon Ionisation Cooling Experiment," *Eur. Phys. J.* **C73** no. 10, (2013) 2582, arXiv:1306.1509 [physics.acc-ph].

[18] **Mice Collaboration** Collaboration, R. Bertoni *et al.*, "The design and commissioning of the MICE upstream time-of-flight system," *Nucl.Instrum.Meth.* **A615** (2010) 14–26, arXiv:1001.4426 [physics.ins-det].

[19] R. Bertoni, M. Bonesini, A. de Bari, G. Cecchet, Y. Karadzhov, and R. Mazza, "The construction of the MICE TOF2 detector." http://mice.iit.edu/micenotes/public/pdf/MICE0286/MICE0286.pdf, 2010.

[20] L. Cremaldi, D. A. Sanders, P. Sonnek, D. J. Summers, and J. Reidy, Jr, "A Cherenkov Radiation Detector with High Density Aerogels," *IEEE Trans. Nucl. Sci.* **56** (2009) 1475–1478, arXiv:0905.3411 [physics.ins-det].

[21] M. Ellis *et al.*, "The design, construction and performance of the MICE scintillating fibre trackers," *Nucl. Instrum. Meth.* **A659** (2011) 136–153, arXiv:1005.3491 [physics.ins-det].

[22] F. Ambrosino *et al.*, "Calibration and performances of the KLOE calorimeter," *Nucl. Instrum. Meth.* **A598** (2009) 239–243.

[23] R. Asfandiyarov *et al.*, "The design and construction of the MICE Electron-Muon Ranger," *JINST* **11** no. 10, (2016) T10007, arXiv:1607.04955 [physics.ins-det].

[24] S. Blot, "Proton Contamination Studies in the MICE Muon Beam Line," *Proceedings 2nd International Particle Accelerator Conference (IPAC 11) 4-9 September 2011, San Sebastian, Spain* (2011) .

[25] **GEANT4** Collaboration, S. Agostinelli *et al.*, "Geant4: A simulation toolkit," *Nuclear Instruments and Methods in Physics Research A* **506** (2003) 250–303.

[26] J. Allison *et al.*, "Geant4 developments and applications," *IEEE Trans. Nucl. Sci.* **53** (2006) 270–278.

[27] R. Brun and F. Rademakers, "ROOT: An object oriented data analysis framework," *Nucl. Instrum. Meth.* **A389** (1997) 81–86.